

Defne Bayraktar · Stefan Diethelm · Peter Holtappels ·  
Thomas Graule · Jan Van herle

## Oxygen transport in $\text{La}_{0.5}\text{Sr}_{0.5}\text{Fe}_{1-y}\text{Ti}_y\text{O}_{3-\delta}$ ( $y=0.0, 0.2$ ) membranes

Received: 24 December 2005 / Accepted: 20 January 2006 / Published online: 21 March 2006  
© Springer-Verlag 2006

**Abstract** The influence of partial substitution of Fe with Ti on the oxygen transport properties of  $\text{La}_{1-x}\text{Sr}_x\text{FeO}_3$  membranes was investigated in view of their application for oxygen separation. Samples of composition  $\text{La}_{0.5}\text{Sr}_{0.5}\text{Fe}_{1-y}\text{Ti}_y\text{O}_{3-\delta}$  ( $y=0, 0.2$ ) were prepared and their oxygen transport properties characterised by potential step relaxation and by oxygen permeation measurement in an air/argon gradient. With the first technique, chemical diffusion ( $\tilde{D}$ ) and surface exchange ( $k_S$ ) coefficients were obtained by fitting of the current relaxation data to a single expression valid over the complete time range. The Ti-substituted composition gave slightly larger values of  $\tilde{D}$  and  $k_S$ . The trend was opposite for the measured oxygen permeation flux. In the latter experience, ordering of oxygen vacancies was observed at lower temperature, reducing significantly the performance of the material.

**Keywords** Chemical diffusion · Mixed electronic–ionic conductors · Oxygen permeation · Perovskites · Vacancy ordering

---

D. Bayraktar · P. Holtappels · T. Graule  
Laboratory for High Performance Ceramics,  
Empa Materials Science and Technology,  
Ueberlandstr. 129,  
8600 Dübendorf, Switzerland

S. Diethelm (✉)  
HTceramix SA,  
av. des Sports 26,  
1400 Yverdon-les-Bains, Switzerland  
e-mail: stefan.diethelm@epfl.ch  
Tel.: +41-21-6935869  
Fax: +41-21-6933502

J. Van herle  
Laboratory for Industrial Energy Systems (LENI), STI, Ecole Polytechnique Fédérale de Lausanne (EPFL),  
1015 Lausanne, Switzerland

### Introduction

Significant research has been done on perovskite-type mixed conducting oxide ceramics considering the applications such as electrode materials for solid oxide fuel cells or oxygen separation membranes [1–6]. The ability of such compositions to tolerate a high amount of non-stoichiometry with acceptor doping allows them to exhibit high permeation flux as first investigated by Teraoka et al. [3, 4].  $(\text{La}, \text{Sr})\text{FeO}_3$ -based materials have been studied extensively [7–12] and considered to be promising for applications as oxygen separation membrane for partial oxidation of methane to syngas, where the materials are required to possess high permeation flux together with good chemical and structural stability over a wide range of oxygen partial pressure ( $p(\text{O}_2)$ ) [13]. The stability of the materials is commonly improved by B-site doping with a more stable cation such as Cr, Al, Ga, etc. [11, 14–17]. However, most of the additions are reported to cause a decrease in ionic conductivity.

In search of a suitable material for the mentioned applications of these perovskite materials, it is important to know their transport properties, including surface exchange and diffusion rates of oxygen at operating conditions and the permeation rate in a  $p(\text{O}_2)$  gradient. The latter is important to know the total response of the material in certain conditions. However, a more detailed information (e.g. the limiting factor for oxygen permeation) can be obtained by commonly used relaxation techniques [18–21].

In this work,  $(\text{La}, \text{Sr})\text{FeO}_{3-\delta}$  with 50% Sr on the A-site was chosen as the base material, which was reported to have the highest ionic conductivity in this series of materials [7]. In addition, Ti was used as a dopant on the B-site for stabilisation. Previous work conducted on similar materials showed that Ti-doping on the B-site decreases oxygen permeability and total conductivity and, at the same time, the thermal expansion [11, 15]. In the present study, the influence of Ti-substitution on the transport

properties of  $(\text{La}, \text{Sr})\text{FeO}_{3-\delta}$  materials is studied in a more comprehensive manner.

## Experimental

### Sample preparation

$\text{La}_{0.5}\text{Sr}_{0.5}\text{FeO}_{3-\delta}$  and  $\text{La}_{0.5}\text{Sr}_{0.5}\text{Fe}_{0.8}\text{Ti}_{0.2}\text{O}_{3-\delta}$  powders (abbreviated as LSF and LSFT2, respectively) were prepared by solid state reaction from  $\text{La}(\text{OH})_3$ ,  $\text{SrCO}_3$ ,  $\text{Fe}_2\text{O}_3$ , and  $\text{TiO}_2$ . The starting powders were mixed by ball-milling for 24 h followed by spray drying and calcining at 1,523 K for 4 h. The spray-dried powders were reground via ball-milling to obtain an average particle size in the range of 1–2  $\mu\text{m}$  as measured by laser scattering. Finally, the powders were spray-dried once more before pressing. Phase purities of the compositions were checked by XRD (X'pert PRO PW3040, PANalytic).

The pellets to be used in electrochemical measurements were prepared by uniaxial pressing with 70 MPa. The pellets were sintered at 1,700 and 1,800 K for LSF and LSFT2, respectively, for 4 h. The optimum sintering temperatures were found by dilatometer experiments. The sintered samples had >95% relative density as measured by Archimedes method. The pellets for electrochemical and permeation measurements were prepared by polishing their surfaces down to 2,500 grit SiC paper.

### Potential-step measurement

A full description of the electrochemical cell used with the potential step (PS) technique for the characterisation of oxygen transport in mixed conducting oxides is given elsewhere [19]. Figure 1 gives a schematic representation of the electrochemical cell used in this study for the potential step experiments. The sample pellet (~8 mm diameter) is interfaced on one side with an oxygen pump consisting of a YSZ slab with Pt electrodes. The upper electrode is electrically contacted through a gold ring that also acts as a spacer between the sample and the oxygen pump. The top and lateral surfaces of the sample are coated with gold paste and are sealed with glass. The gold coating prevents reaction between the glass and the sample. After assembling the sample with the oxygen pump, the cell was first heated up rapidly to burn the organics and densify the

gold coating. After cooling, the glass sealing was added and the cell reheated to 950°C for measurement.

The principle of the measurement is to apply a voltage step across the YSZ slab, which corresponds to a change in the oxygen partial pressure ( $p(\text{O}_2)$ ) at the surface of the sample. The sample then equilibrates with this new surrounding atmosphere through solid state diffusion of oxygen. This equilibration results in an electrical current through the oxygen pump to maintain constant the oxygen concentration within the gas space.

The measurement sequence followed in this work was to apply first a -20 mV vs air potential step, followed by a -20→0 mV potential step, therefore, measuring the equilibration kinetics for both reduction and oxidation. The cell was then cooled down to the next temperature and the same sequence was applied. At each step, the decay of the relaxation current to 0 (i.e. a few microamperes) was taken as an indication of equilibrium. At a given temperature, the applied potential was also increased step-wise up to -100 mV vs air to observe the evolution of the oxygen transport parameters with varying  $p(\text{O}_2)$ .

### Permeation measurements

For the oxygen permeation measurements, the samples were characterised as Ø25-mm discs, clamped between two alumina tubes with gold rings as sealings [22]. Air (50 ml/min) was flown on one side and argon (100 ml/min) on the other. The amount of oxygen that has permeated through the membrane is determined by measuring the outlet argon flow rate with a bubble meter and analysing its composition with a gas chromatograph (Varian) equipped with a molecular sieve 5-Å capillary column [22]. The membrane was initially heated in an air/argon gradient up to 1,050°C to soften the gold and tighten the sealing. The temperature was then decreased to the measurement temperatures.

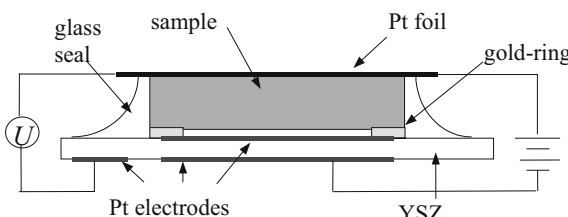
### Electrochemical data analysis

The approach followed in this work for the analysis of the potential step relaxation data differs from that described in previous publications [19, 21]; a single expression, based on asymptotic expressions, but valid over the full time scale, is used to fit the complete data range to extract the oxygen transport parameters. This new approach will be only briefly exposed in this section as a more detailed derivation and discussion is outside the scope of this paper but will be published separately.

The general solution for the current relaxation following a potential step is, in its infinite series form, given by [23]:

$$I(t) = Q \sum_{n=1}^{\infty} \frac{2\Lambda^2 \tilde{D} \exp(-\lambda_n^2 \tilde{D}t/L^2)}{L^2(\lambda_n^2 + \Lambda^2 + \Lambda)} \quad (1)$$

**Fig. 1** Schematic representation of the electrochemical cell used for the potential step measurements



where  $\tilde{D}$  is the chemical diffusion coefficient,  $L$  is the sample thickness,  $Q$  is the total charge passed during the potential step,  $\Lambda = k_T L / \tilde{D}$ , with  $k_T$  the surface exchange coefficient associated with the total electrochemical cell resistance ( $R_T$ ), and  $\lambda_n$  are the roots of the transcendental equation

$$\lambda \tan(\lambda) = \Lambda \quad (2)$$

Equation 1, in its infinite series form, and Eq. 2 are not practical for data analysis; it is, therefore, useful to use approximations for both short and long times [19]. At short time ( $t < t_c \equiv 0.154 L^2 / \tilde{D}$ ), the relaxation current can be described by [24]

$$I(t) = \frac{Qk_T}{L} \left[ \frac{R_S}{R_T - R_S} \exp\left(-\frac{t}{\tau_g}\right) + \exp\left(\frac{t}{\tau_d}\right) \operatorname{erfc}\left(\sqrt{\frac{t}{\tau_d}}\right) \right] \quad (3)$$

where  $\tau_d = \tilde{D}/k_T^2$  is the time constant associated with the diffusion process,  $\tau_g$  is the time constant of the oxygen pump response and  $R_S$  is the resistance associated with the surface exchange reaction. The first exponential term in Eq. 3 corresponds to the rapid response of the oxygen pump and gas space to a potential step, whereas the second term describes the diffusion process [24]. The latter is analogous to the expression used for analysing depth profiles in isotopic exchange experiments, which describes diffusion in a semi-infinite media with linear surface exchange boundary conditions [25].

At large time ( $t > t_c$ ), the relaxation current can be described by an appropriate number of terms of Eq. 1. It can be shown that the two first terms are sufficient to obtain a consequent overlap between the long- and short-time expressions (Eqs. 1 and 3) around  $t=t_c$ . The use of Eq. 1 requires the simultaneous determination of the roots of Eq. 2. Although a numerical routine has been proposed for this calculation [26], it is still useful to work with an explicit expression of those roots. An approximation for  $\lambda_1$  was first given in [24]:

$$\lambda_1 = \sqrt{\frac{\Lambda}{1 + \Lambda/3}} \quad (4)$$

For the other roots, Eq. 2 was linearised to obtain

$$\lambda_n = (n-1)\pi \left( 1 + \frac{\Lambda}{\Lambda + (n-1)^2 \pi^2} \right) \text{ for } n > 1 \quad (5)$$

These approximations are accurate within  $<1\%$  for  $\Lambda \leq 1$ . As we will see below, this condition is practically always fulfilled for the data obtained in this study.

Finally, the current relaxation data could be fitted over the complete time domain (four decades of time scale) to a hybrid solution matching Eqs. 1 and 3 at  $t=t_c$ . The fits were performed using the NLLS fitting algorithm of ORIGIN (OriginLab Corporation, Northampton, MA, USA).

## Results and discussion

### Potential step data

The relaxation currents after a  $-20\text{-mV}$  potential vs air step at different temperatures are shown in Fig. 2, along with the best fits to the hybrid solution. The data have been plotted with a logarithmic time scale to show the quality of the fit over the complete time domain. However, when plotted with a logarithmic current scale, the current responses show a typical exponential decay after a few hundreds of seconds. The response of the oxygen pump vanishes after a few tens of seconds giving way to the response of the sample. The respective time constants of the two processes ( $\tau_g$  and  $\tau_d$ , respectively) are given in Table 1 for different temperatures, along with the switch time ( $t_c$ ) between the short- and long-time behaviour. It can be seen that  $\tau_g$  increases with decreasing temperature due to the combined increase of the gas space capacity and interfacial resistance [24]. It is important that  $\tau_g \ll t_c$  for the purpose of analysis, otherwise the response of the oxygen pump could hinder the evaluation of the transport parameters. This problem is similar to that of the reactor time lag in conductivity relaxation measurements as discussed by den Otter et al. [27]. In the same table, the values of the constant  $\Lambda (= k_T L / \tilde{D})$  and of the critical thickness ( $L_c = \tilde{D} / k_S$ ) are also given for all temperatures.  $L_c$  corresponds to the thickness of the sample below which the transport of oxygen becomes limited by surface exchange. It can be seen that  $L_c$  increases as the

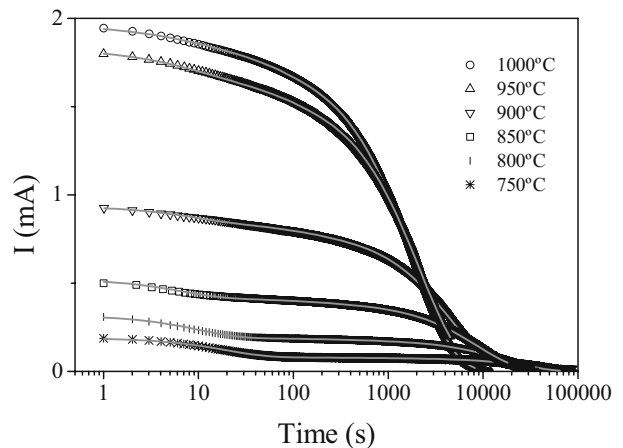


**Fig. 2** Current relaxation data for LSF in response to  $-20\text{ mV}$  vs air potential steps at various temperatures. The grey lines are the best fits using the hybrid expression combining Eq. 3 and the two first terms of Eq. 1

**Table 1** Temperature dependence of time constants related to the gas composition change ( $\tau_g$ ) and the diffusion process ( $\tau_d$ ), and of the time boundary between short- and long-time expressions  $t_c$

T (°C)	$t_c$ (s)	$\tau_g$ (s)	$\tau_d$ (s)	$\Lambda$	$L_c$ (mm)
1,000	150	3.1	1,700	0.76	0.06
950	145	2.7	1,789	0.73	0.07
900	296	3.0	4,528	0.65	0.29
850	632	4.9	9,087	0.67	0.49
800	1,432	9.1	17,383	0.73	0.62
750	1,984	19.7	50,847	0.50	1.08

temperature decreases, indicating that the oxygen transport in the sample becomes surface limited at low temperature. On the other hand, the constant  $\Lambda$  remains smaller than 1 over the complete experimental range, therefore satisfying the validity criteria for the approximations 4 and 5.

In Fig. 3, it is interesting to notice that the response to a reduction step (0→−20 mV) differs from that of an oxidation step (−20→0 mV). The chemical diffusion ( $\tilde{D}$ ) and surface exchange ( $k_s$ ) coefficients, obtained from the fits for the two compositions, are displayed as Arrhenius plots in Figs. 4 and 5, respectively. In each figure, the data for both reduction and oxidation runs are given and the corresponding activation energies ( $E_A$ ) are reported in Table 2. The oxidation data is systematically higher than the reduction data. Moreover, the oxygen transport parameters are slightly higher for LSFT2 than LSF. This difference is, at first sight, surprising but it can be explained from the difference in concentration of the mobile species between the two compositions. For small defect concentrations (as it is the case in air), the chemical diffusion coefficient is inversely proportional to the mole fraction of defects [28]; it will, therefore, be higher in LSFT2 than in LSF.

Current relaxation data obtained at 1,000°C by increasing stepwise the applied potential across a LSF sample

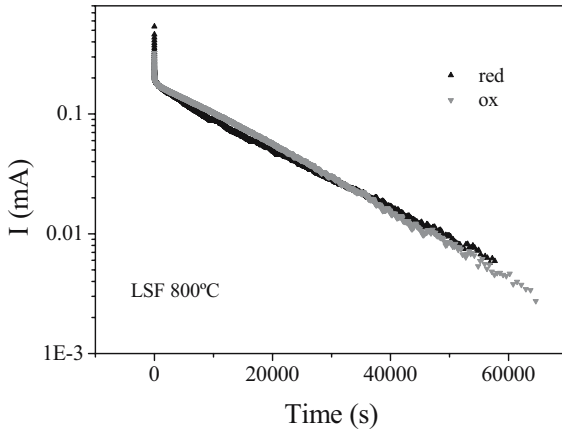


**Fig. 3** Current relaxation data for LSF at 800°C, in response to a 0→−20 mV vs air reduction step (red) and to a −20→0 mV vs air oxidation step (ox)

from 0 to −100 mV vs air are shown in Fig. 6. As after each step equilibrium is reached (i.e. the current decays to 0), the corresponding oxygen partial pressure can be evaluated using Nernst law. The resulting oxygen transport coefficients ( $\tilde{D}$  and  $k_s$ ) are given in Fig. 7, showing their  $p(O_2)$  dependence. The data obtained similarly by consecutive oxidation steps are also displayed. Close to 0 bias, i.e. in air, both  $\tilde{D}$  and  $k_s$  obtained from oxidation runs are higher than for the reduction run, which is consistent with the data in Figs. 4 and 5; but, as the voltage is increased negatively, i.e. as the  $p(O_2)$  is lowered, the tendency is reversed for  $k_s$ . Both  $k_s$  and  $\tilde{D}$  tend to decrease with decreasing  $p(O_2)$ , following approximately a  $\sqrt{p(O_2)}$  trend. This behaviour of  $k_s$  was previously observed in  $SrFe_{0.5}Co_{0.5}O_{3-\delta}$  and attributed to the kinetics of oxygen incorporation [24].

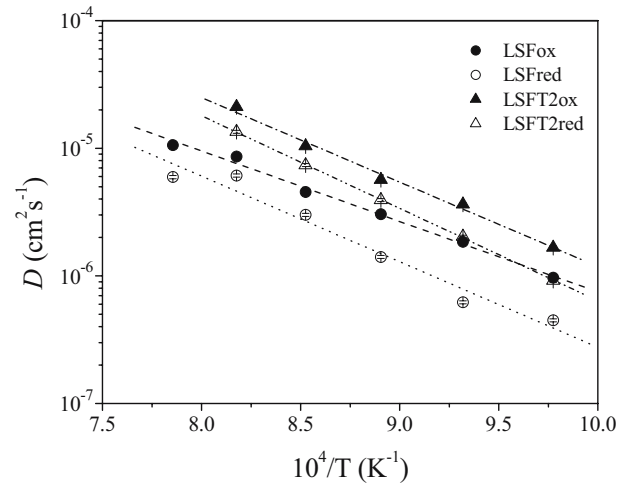


**Fig. 4** Arrhenius plot of the chemical diffusion coefficients ( $\tilde{D}$ ) obtained by fitting the current relaxation data

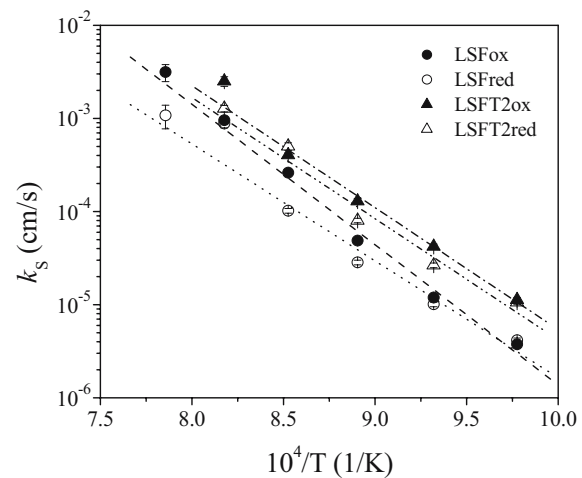


**Fig. 5** Arrhenius plot of the surface exchange coefficients ( $k_s$ ) obtained by fitting the current relaxation data

**Table 2** Oxygen transport data for LSF and LSFT2 obtained from fitting

Composition	Voltage step (mV)	$D_{900^\circ\text{C}}$ ( $\text{cm}^2/\text{s}$ )	$E_{A,D}$ (kJ/mol)	$k_{S,900^\circ\text{C}}$ ( $\text{cm}/\text{s}$ )	$E_{A,k}$ (kJ/mol)
LSF	0→-20	$3.01(8) \cdot 10^{-6}$	128(2)	$1.02(6) \cdot 10^{-4}$	240(5)
	-20→0	$4.5(1) \cdot 10^{-6}$	106(2)	$2.6(2) \cdot 10^{-4}$	288(4)
LSFT2	0→-20	$7.4(2) \cdot 10^{-6}$	139(2)	$5.0(4) \cdot 10^{-4}$	249(5)
	-20→0	$1.04(3) \cdot 10^{-5}$	126(2)	$4.1(2) \cdot 10^{-4}$	251(5)

The number between brackets indicates the uncertainty on the last digit

### Permeation data

After each change in temperature, the oxygen flux took some time to settle, from a few hours at high temperature ( $>900^\circ\text{C}$ ) to a few days at lower temperature ( $<850^\circ\text{C}$ ). In addition, the equilibration time was systematically longer after a heating step than after a cooling step. This latter result is consistent with the kinetical difference between oxidation and reduction steps mentioned in the previous section for the potential step measurement. During cooling, the membrane takes oxygen in to maintain its equilibrium oxygen concentration, which corresponds to an oxidation process. On the contrary, during heating, the membrane releases oxygen, which corresponds to a reduction process. Beyond the consistency between the different experiments, this kinetical difference between oxidation and reduction will be discussed further below.

The slow equilibration of the permeation flux through a LSF membrane after a heating step from 750 to  $950^\circ\text{C}$  is shown in Fig. 8. In all cases, the settlement value of the flux was taken as its equilibrated value.

The equilibrated oxygen permeation data for both compositions are shown in an Arrhenius plot (Fig. 9). To allow direct comparison, the values were normalised by multiplying the fluxes by the membrane thickness expressed in millimeters. Doing so, it is of course assumed that the oxygen transport through the membrane is governed by bulk diffusion. The LSF data are higher than the LSFT2 data. This result is consistent with data reported in literature for similar compositions [11]. The partial substitution of Fe with Ti decreases the concentra-

tion of oxygen vacancies that are the mobile species and, thus, reduces both the electronic and the ionic conductivities [11, 29]. Furthermore, the LSFT2 data present a discontinuity around  $875^\circ\text{C}$ , which corresponds to the temperature below which the equilibration of the flux becomes very slow. Kruidhof et al. [30] reported a similar

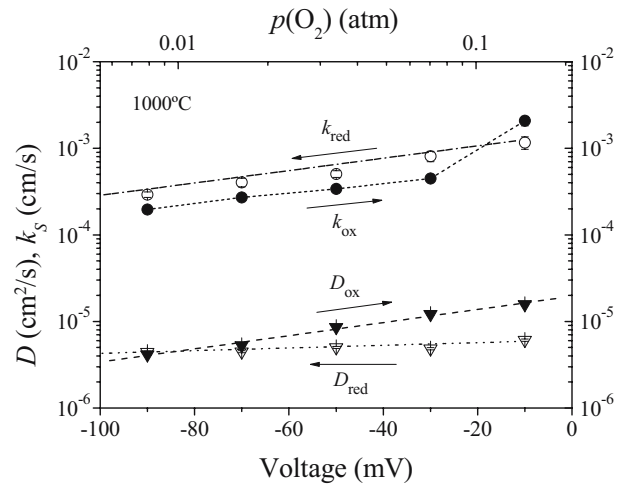


**Fig. 7** Evolution of the chemical diffusion ( $\tilde{D}$ ) and surface exchange ( $k_s$ ) coefficients with increasing voltage bias resulting from consecutive -20-mV potential steps down to -100 mV (red) and back to 0 mV (ox)

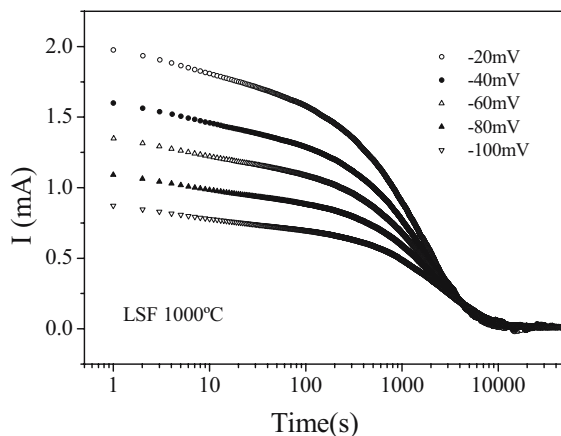


**Fig. 6** Current relaxation data for LSF at  $1,000^\circ\text{C}$ , resulting from consecutive -20-mV potential steps down to -100 mV

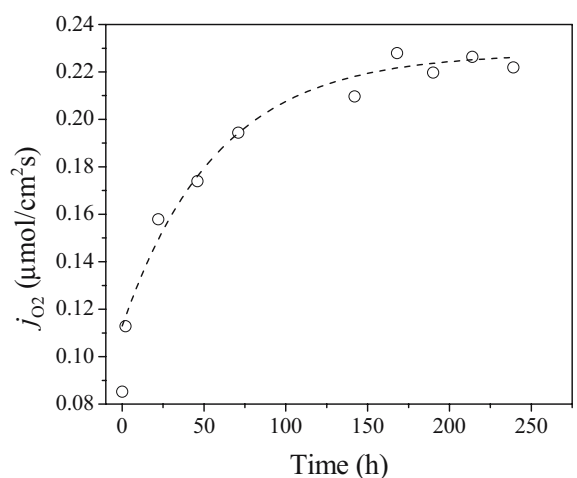


**Fig. 8** Slow equilibration of the oxygen permeation flux through a LSF membrane in an air/argon gradient consecutive to an increase in temperature from  $750$  to  $950^\circ\text{C}$

behaviour for  $\text{SrCo}_{0.8}\text{Fe}_{0.2}\text{O}_{3-\delta}$  and attributed it to an order-disorder transformation, from the high-temperature perovskite phase, where the oxygen vacancies are distributed randomly, to the lower temperature brownmillerite phase, where the vacancies are ordered and, thus, less mobile [30]. Such behaviour is not clearly apparent for LSF, even though a change in the activation energy occurs in the same temperature range. A slow equilibration in LSF and LSFT2 has already been reported by other groups [7, 11, 29] at intermediate  $p(\text{O}_2)$  ranges ( $10^{-7}$ – $10^{-14}$  atm), but no clear explanation was given. This behaviour could be related to a gradual ordering of oxygen vacancies as discussed by Grenier et al. for  $\text{La}_{1-x}\text{Sr}_x\text{FeO}_3$  and other related compounds such as  $\text{La}_{1-x}\text{Ca}_x\text{FeO}_3$  and  $\text{CaTi}_{1-2y}\text{Fe}_{2y}\text{O}_{3-y}$  [31]. Mössbauer spectroscopy showed that, even at low levels of vacancies, the defects tend to associate, transforming the octahedral site of the transition metal into a tetrahedral site, this despite the maintenance of the pseudo-cubic symmetry observed by XRD. The presence of Fe favours this transformation because it can equally occupy each type of site [32]. On the basis of their observation, Grenier et al. proposed a three-step mechanism for the formation of oxygen non-stoichiometry in Fe-containing perovskites: (1) At low defect levels, the oxygen vacancies align along arrays of variable length oriented randomly along any of the directions of the lattice; (2) At higher levels of defects, the number of arrays with quasi-infinite length increases rapidly and tend to order in parallel lines in microdomains that are randomly distributed; (3) Finally, at the transition non-stoichiometry ( $\delta_c$ ), the number of infinite length vacancy arrays is such that a long-distance order occurs, with the arrays aligned parallel in planes. Beyond  $\delta_c$ , the further increase of vacancies results in a gradual increase of the number of vacancy planes (tetrahedral) relative to the octahedral planes. This long-range order leads to new crystalline structures made of intergrowth of the perovskite and the brownmillerite phases.

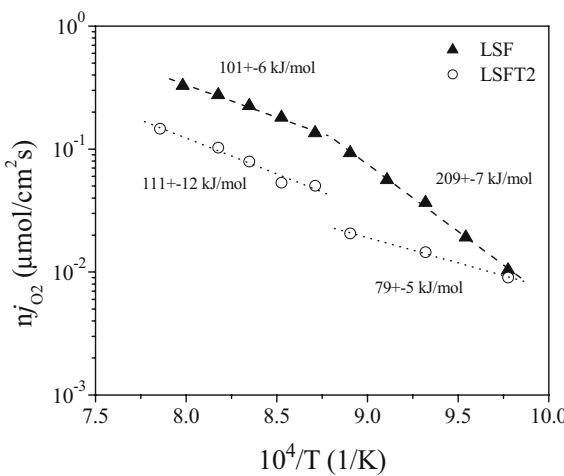


**Fig. 9** Arrhenius plot of the equilibrated values of the normalised oxygen permeation flux through LSF and LSFT2 membranes. The numbers in the figure indicate the values of the activation energies

An association of vacancies is expected to reduce their mobility or to reduce the concentration of mobile species. This is expected to have an important influence on the ionic conductivity which is proportional to the concentration of mobile species and the mobility and, thus, on the oxygen flux. This mechanism also sheds light on the difference between the kinetics of oxidation and reduction: during reduction, oxygen vacancies are formed that tend to associate to some extent, lowering their mobility. On the contrary, vacancies are disassembled during oxidation, thus, enhancing their mobility.

To evaluate the temperature and  $p(\text{O}_2)$  conditions in which such an order-disorder transition would occur, an approximate phase diagram was established on the basis of the observations reported by Grenier et al. [31]. The critical oxygen non-stoichiometry ( $\delta_c$ ) beyond which ordering occurs was determined from the structural evolution of various compositions of LSF annealed at different temperatures. The temperature dependence of  $\delta_c$  is shown in Fig. 10 along with the diagram. For each value of  $\delta_c$ , the corresponding  $p(\text{O}_2)$  was determined for LSF using the data from the work of Mizusaki et al. [10]. According to this approximate diagram, the transition occurs at more reducing  $p(\text{O}_2)$  as the temperature is increased. Below  $850^\circ\text{C}$ , the critical  $p(\text{O}_2)$  is around  $10^{-6}$  atm, which is close to the value obtainable in an air/argon gradient. It is, therefore, possible that such an order-disorder transition occurs during the permeation experiment in an air/argon gradient.

#### Ionic conductivity calculations

Values of the ionic conductivity ( $\sigma_i$ ) can be calculated from the data of both current relaxation and permeation measurement providing some assumptions. For a predom-

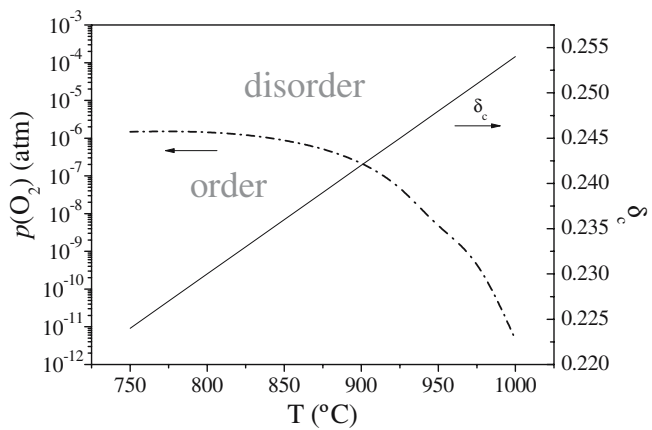


**Fig. 10** Phase diagram for the order-disorder transition in LSF with the values of the critical oxygen nonstoichiometry taken from [31]

inantly electronic conductor ( $\sigma_e \gg \sigma_i$ ), the ionic conductivity is related to the chemical diffusion coefficient through [21]

$$\sigma_i = -\frac{8F^2}{RTV_m} \frac{d\delta}{d \ln p(O_2)} \tilde{D} \cong \frac{\Delta Q}{V \Delta E} \tilde{D} \quad (6)$$

where  $F$  is Faraday's constant,  $R$  is the ideal gas constant,  $V_m$  is the molecular volume of the sample,  $V$  its volume, and  $d\delta/d \ln p(O_2)$  is the slope of the oxygen non-stoichiometry data vs  $p(O_2)$ . In the right-hand side of Eq. 6, the latter has been evaluated from the amount of charge  $\Delta Q$  extracted from (or incorporated in) the sample during  $\Delta E$  potential step [21].

If one similarly assumes that the oxygen transport through the permeation membrane is bulk limited, an average ionic conductivity can be calculated from the permeation flux ( $j_{O_2}$ ) [12]:

$$\sigma_i = -\frac{16F^2 L}{RT \Delta \ln(p(O_2))} j_{O_2} \quad (7)$$

Figure 11 compares the ionic conductivity calculated both ways for both compositions. For LSF, the results are consistent given the fact that the relaxation data were measured in air whereas the permeation data correspond to averaged values over an air/argon gradient. On the contrary, the LSFT2 values differ significantly. This indicates that oxygen transport in LSFT2 is strongly lowered in more reducing conditions, probably due to the ordering of the oxygen vacancies. This would prevent its use as an oxygen permeation membrane, especially for partial oxidation reactor application. However, these conclusions remain speculative and further investigations are still required for a full understanding of oxygen transport in Ti-substituted LSF in large  $p(O_2)$  gradients.

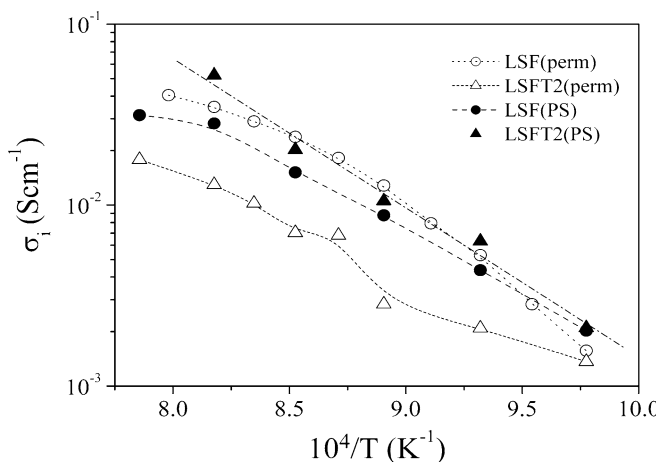


**Fig. 11** Comparison between the values of the ionic conductivity ( $\sigma_i$ ) calculated for both compositions from the potential step (PS) data using Eq. 6 and from the permeation data (perm) using Eq. 7

## Conclusions

The oxygen transport properties of  $\text{La}_{0.5}\text{Sr}_{0.5}\text{FeO}_3$  and  $\text{La}_{0.5}\text{Sr}_{0.5}\text{Fe}_{0.8}\text{Ti}_{0.2}\text{O}_3$  were investigated by current relaxation and permeation measurement. Chemical diffusion ( $\tilde{D}$ ) and surface exchange ( $k_s$ ) coefficients were obtained as a function of temperature by fitting the relaxation data over the complete time range (four decades of time range). Both  $\tilde{D}$  and  $k_s$  values in air for LSFT2 were slightly larger than for LSF. This difference can be explained in terms of the difference in concentration of oxygen vacancies as at low concentrations; the thermodynamic factor is inversely proportional to the molar fraction. The trend was opposite for the permeation data. The oxygen flux through a LSF membrane placed between air and argon was a factor of 3 higher than through LSFT2. Furthermore, some evidence of oxygen vacancy ordering was observed in the permeation data, especially for LSFT2, resulting in a reduction of the oxygen flux. Such behaviour is prejudicial for the use of these materials as oxygen separation membrane, especially in large oxygen partial pressure gradients.

**Acknowledgement** This work was supported by the Swiss National Science Foundation (Project nos. 200021-100674/1 and 200020-109643/1).

## References

- Hammou A, Guindet J (1997) Solid oxide fuel cells. In: Gellings PJ, Bouwmeester HJM (eds) CRC handbook of solid state electrochemistry. CRC, Boca Raton, pp 413–420
- Bouwmeester HJM, Burggraaf AJ (1997) Dense ceramic membranes for oxygen separation. In: Gellings PJ, Bouwmeester HJM (eds) CRC handbook of solid state electrochemistry. CRC, Boca Raton, pp 519–542
- Teraoka Y, Zhang HM, Furukawa S, Yamazoe N (1985) Chem Lett 1743
- Teraoka Y, Zhang HM, Okamoto K, Yamazoe N (1988) Mater Res Bull 23:51
- Steele BCH (2000) Dense ceramic ion conducting membranes. In: Tuller HL (ed) Oxygen ion and mixed conductors and their technological applications, series E, vol 368. Nato ASI Series, pp 323–345
- Ullmann H, Trofimenco N (1999) Solid State Ion 119:1
- Patrakeev MV, Bahteeva JA, Mitberg EB, Leonidov IA, Kozhevnikov VL, Poeppelmeier KR (2003) J Solid State Chem 172:219
- ten Elshof JE, Bouwmeester HJM, Verweij H (1995) Solid State Ion 81:97
- ten Elshof JE, Bouwmeester HJM, Verweif H (1996) Solid State Ion 89:81
- Mizusaki M, Yoshihiro M, Yamauchi S, Fueki K (1985) J Solid State Chem 58:257
- Tsipis EV, Patrakeev MV, Kharton VV, Yaremchenko AA, Mather GC, Shaula AL, Leonidov IA, Kozhevnikov VL, Frade JR (2005) Solid State Ion 7:355
- Diethelm S, Van herle J, Sfeir J, Buffat P (2004) Br Ceram Trans 103:147
- Hendriksen PV, Larsen PH, Mogensen M, Poulsen FW, Wiik K (2000) Catal Today 56:283
- Kharton VV, Shaula AL, Snijkers FMM, Cooymans JFC, Luyten JJ, Yaremchenko AA, Valente AA, Tsipis EV, Frade JR, Marques FMB, Rocha J (2005) J Membr Sci 252:215

15. Fagg DP, Kharton VV, Frade JR, Ferreira AAL (2003) Solid State Ion 156:45
16. Yaremenko AA, Patrakeev MV, Kharton VV, Marques FMB, Leonidov IA, Kozhevnikov VL (2004) Solid State Ion 6:357
17. Atkinson A, Ramos TMGM (2000) Solid State Ion 129:259
18. Belzner A, Gür TM, Huggins RA (1990) Solid State Ion 40/41:353
19. Diethelm S, Closset A, Nisancioglu K, Van herle J, McEvoy AJ, Gür TM (1999) J Electrochem Soc 146:2606
20. Bucher E, Benisek A, Sitte W (2003) Solid State Ion 157:39
21. Diethelm S, Van herle J (2004) Solid State Ion 174:127
22. Diethelm S, Sfeir J, Clemens F, Van herle J, Favrat D (2004) J Solid State Electrochem 8:611
23. Crank J (1975) The mathematics of diffusion, 2nd edn. Clarendon, Oxford, p 60
24. Diethelm S, Closset A, Van herle J, Nisancioglu K (2002) J Electrochem Soc 149:E424
25. Carslaw HS, Jaeger JC (1959) Conduction of heat in solids, 2nd edn. Oxford Univ. Press, London, p 70
26. den Otter MW, van der Haar LM, Bouwmeester HJM (2000) Solid State Ion 134:259
27. den Otter MW, Bouwmeester HJM, Boukamp BA, Verweij H (2001) J Electrochem Soc 148:J1
28. Maier J (1993) J Am Ceram Soc 76:1212
29. Park CY, Jacobson AJ (2005) J Electrochem Soc 152:J65
30. Kruidhof H, Bouwmeester HJM, v Dorn RHE, Burggraaf AJ (1993) Solid State Ion 63–65:816
31. Grenier JC, Pouchard M, Hagenmuller P, Komornicki S (1980) Order-disorder phenomena in some oxygen-deficient perovskite-related ferrites. In: Proceedings of the international conference on ferrites, Japan, p 410
32. Grenier JC, Menil F, Pouchard M, Hagenmuller P (1978) Mater Res Bull 13:329